

Synthesis of two-dimensional diamond by phase transition from graphene at atmospheric pressure

Songyang Li(李松洋), Zhiguang Zhu(朱志光), Youzhi Zhang(张有志), Chengke Chen(陈成克), and Xiaojun Hu(胡晓君)

Citation: Chin. Phys. B, 2025, 34 (**5**): 058101. DOI: 10.1088/1674-1056/adb688
http://cpb.iphy.ac.cn; http://iopscience.iop.org/cpb

What follows is a list of articles you may be interested in

Unravelling biotoxicity of graphdiyne: Molecular dynamics simulation of the interaction between villin headpiece protein and graphdiyne

Bei-Wei Zhang(张贝薇), Bing-Quan Zhang(张兵权), Zhi-Gang Shao(邵志刚), and Xianqiu Wu(吴先球)
Chin. Phys. B, 2024, 33 (**11**): 118102. DOI: 10.1088/1674-1056/ad7af5

Bimodal growth of Fe islands on graphene

Yi-Sheng Gu(顾翊晟), Qiao-Yan Yu(俞俏滟), Dang Liu(刘荡), Ji-Ce Sun(孙蓟策), Rui-Jun Xi(席瑞骏), Xing-Sen Chen(陈星森), Sha-Sha Xue(薛莎莎), Yi Zhang(章毅), Xian Du(杜宪), Xu-Hui Ning(宁旭辉), Hao Yang(杨浩), Dan-Dan Guan(管丹丹), Xiao-Xue Liu(刘晓雪), Liang Liu(刘亮), Yao-Yi Li(李耀义), Shi-Yong Wang(王世勇), Can-Hua Liu(刘灿华), Hao Zheng(郑浩), and Jin-Feng Jia(贾金锋)
Chin. Phys. B, 2024, 33 (**6**): 068104. DOI: 10.1088/1674-1056/ad322f

Effect of external magnetic field on the instability of THz plasma waves in nanoscale graphene field-effect transistors

Liping Zhang(张丽萍), Zongyao Sun(孙宗耀), Jiani Li(李佳妮), and Junyan Su(苏俊燕)
Chin. Phys. B, 2024, 33 (**4**): 048102. DOI: 10.1088/1674-1056/ad1e66

Intercalation of hafnium oxide between epitaxially-grown monolayer graphene and Ir(111) substrate

Yi Biao(表奕), Hong-Liang Lu(路红亮), Hao Peng(彭浩), Zhi-Peng Song(宋志朋), Hui Guo(郭辉), and Xiao Lin(林晓)
Chin. Phys. B, 2023, 32 (**9**): 098102. DOI: 10.1088/1674-1056/accff4

Morphological features and nanostructures generated during SiC graphitization process

Wen-Xia Kong(孔雯霞), Yong Duan(端勇), Jin-Zhe Zhang(章晋哲),Jian-Xin Wang(王剑心), and Qun Cai(蔡群)
Chin. Phys. B, 2023, 32 (**6**): 068103. DOI: 10.1088/1674-1056/acb766

Synthesis of two-dimensional diamond by phase transition from graphene at atmospheric pressure

Songyang Li(李松洋)[1,2,3,4], Zhiguang Zhu(朱志光)[1,2,3,4], Youzhi Zhang(张有志)[1,2,3,4], Chengke Chen(陈成克)[1,2,3,4], and Xiaojun Hu(胡晓君)[1,2,3,4,†]

[1]*College of Materials Science and Engineering, Zhejiang University of Technology, Hangzhou* 310014, *China*
[2]*Moganshan Diamond Research Center, Huzhou* 313200, *China*
[3]*Diamond Joint Research Center for Zhejiang University of Technology and Tanghe Scientific & Technology Company, Huzhou* 313200, *China*
[4]*Moganshan Institute Zhejiang University of Technology, Huzhou* 313200, *China*

(Received 7 December 2024; revised manuscript received 8 February 2025; accepted manuscript online 17 February 2025)

It is a key challenge to prepare two-dimensional diamond (2D-diamond). Herein, we develop a method for synthesizing 2D-diamond by depositing monodisperse tantalum (Ta) atoms onto graphene substrates using a hot-filament chemical vapor deposition setup, followed by annealing treatment under different temperatures at ambient pressure. The results indicate that when the annealing temperature increases from 700 °C to 1000 °C, the size of the 2D-diamond found in the samples gradually increases from close to 20 nm to around 30 nm. Meanwhile, the size and number of amorphous carbon spheres and Ta-containing compounds between the graphene layers gradually increase. As the annealing temperature continues to rise to 1100 °C, a significant aggregation of Ta-containing compounds is observed in the samples, with no diamond structure detected. This further confirms that monodisperse Ta atoms play a key role in graphene phase transition into 2D-diamond. This study provides a novel method for the ambient-pressure phase transition of graphene into 2D-diamond.

Keywords: graphene, two-dimensional diamond, vacuum annealing, phase transition

PACS: 81.05.ug, 81.15.Gh, 81.16.–c, 83.10.Tv

DOI: 10.1088/1674-1056/adb688 **CSTR:** 32038.14.CPB.adb688

1. Introduction

As an important wide bandgap semiconductor material, diamond is a three-dimensional crystal structure composed of carbon atoms connected to each other by sp^3 bonds, which has superior properties such as high hardness (about 90 GPa), wide bandgap (5.47 eV), high carrier mobility (4600 cm^2/V), high thermal stability, negative electron affinity, and chemical inertness. It showed a wide range of potential in a variety of applications, such as semiconductors,[1] quantum computers,[2] high-performance radiation (particle) detectors,[3] and more. As the size of diamond crystals decreased to nanometer scale, size effect, quantum effect and surface effect induced by the dimensional changes produced many unique properties that were not found in traditional bulk materials.[4,5] The two-dimensional diamond (2D-diamond) is a two-dimensional (2D) carbon material with sp^3 hybrid structure, which has unique physical properties of atomic-scale ultra-thin diamond nanofilms, and has a variety of excellent properties of bulk diamond, such as excellent mechanical, physical and electrical properties.[6–11] Therefore, the research and application of 2D-diamond have become a new development direction in the field of diamond. However, the difficulty of preparing 2D-diamond limits its further research and application.

The 2D-diamond is possible to be prepared by controlling surface chemistry, interfacial interactions, and local strain distributions.[12] It was reported that hydrogenation treatment had been carried out on the surface of monolayer graphene, resulting in a structure similar to hydrogenated monolayer diamond (111), which was named graphane.[13] This provided a reference for the study of 2D-diamond nanofilms. Although the hydrogenation of graphene to synthesize hydrogenated 2D-diamond had been successfully achieved at room temperature and atmospheric pressure,[14] it was difficult to control the hydrogenation rate and defect content. Moreover, there was another challenge to achieve two-sided hydrogenation of graphene, and the gradual dehydrogenation of hydrogenated graphene at room temperature led to a significant decrease in the stability of 2D-diamond.[15–18] Further research reports indicated that when the surface of bilayer graphene or few-layer graphene was functionalized with fluorine atoms, a diamond structure known as fluorinated 2D-diamond (FD) was obtained at relatively low temperatures.[15–17,19] Recently, researchers had successfully synthesized stable fluorinated 2D diamond (FD) on a CuNi(111) substrate by exposing AB-stacked bilayer graphene grown by chemical vapor deposition (CVD) to XeF.[20] However, this method is costly and the fluorination treatment probably makes the 2D-diamond unstable in certain environments, especially at high temperature or strong acid-base conditions, where the fluorinated layer may decompose

†Corresponding author. E-mail: huxj@zjut.edu.cn

© 2025 Chinese Physical Society and IOP Publishing Ltd. All rights, including for text and data mining, AI training, and similar technologies, are reserved.

or react, affecting the properties of the material.

Our group discovered that amorphous carbon or nanographite located at the grain boundaries of nanodiamond films grown by HFCVD underwent a transformation into diamond structure at atmospheric pressure after annealing at temperatures $\leq$ 1000 °C.[21] Building on this foundation, we unveiled the conversion of vertical graphene to diamond in the hot filament chemical vapor deposition (HFCVD) process.[21] Theoretical calculations further reveal that single-side hydrogenated bilayer graphene containing tantalum (Ta) atoms undergoes spontaneous transformation into diamond structures in hydrogen–oxygen atmospheres.[21–23] Notably, recent computational studies demonstrated that transition metals exhibited low adsorption energies and high diffusion barriers on oxygen-terminated diamond substrates, effectively suppressing atomic aggregation while maintaining monodispersed states.[24] These isolated transition metal atoms significantly reduced the energy barrier for the graphite-to-diamond phase transition while releasing substantial energy during the structural reorganization. Moreover, the introduction of tantalum carbide (TaC) exhibited remarkable catalytic efficiency, reducing the required phase transition pressure to only 22.2% of that needed in chemical mediator-free systems. Even under ambient pressure, TaC-mediated systems maintained stable 2D-diamond with minimal residual sp^2-hybridized carbon content.[25]

These provide a theoretical realization for the phase transition from graphene to 2D-diamond. Furthermore, Zhu *et al.*[26] directly deposited tantalum atoms through HFCVD equipment on the surface of high-purity graphite sheets in a minor hydrogen atmosphere, and a large number of diamond particles with sizes ranging from 3 nm to 10 nm were observed in the amorphous carbon layer of the sample, achieving the diamond phase transition of graphite at atmospheric pressure. Recently, in the HFCVD system, the transition from graphite to diamond has been achieved at atmospheric pressure by utilizing monodisperse tantalum atoms generated from tantalum metal wires, yielding diamonds with sizes ranging from 5 nm to 20 nm.[27] This further validated that sp^2 components can transit to sp^3 at atmospheric pressure after the introduction of monodisperse tantalum atoms. Subsequently, Zhu *et al.* prepared vertical graphene sheets containing tantalum atoms via HFCVD and annealed them in an oxygen-containing environment at atmospheric pressure, successfully synthesizing nanodiamond particles with sizes of 2 nm–4 nm primarily distributed within amorphous carbon.[28] The aforementioned results have guided significance for the transition from sp^2 carbon to sp^3 carbon under low-cost and atmospheric pressure conditions, and they provide a new method for the transformation from graphene to diamond. However, the diamond grain sizes obtained in this study were relatively small, and the transition from graphene as a 2D material to diamond in a 2D structure was not achieved.

In this study, a double-helical tantalum wire was utilized to deposit monodisperse tantalum atoms onto graphene precursors via HFCVD equipment, followed by annealing treatment in vacuum under different temperatures to facilitate the phase transition of graphene into diamond within a two-dimensional structure. The results demonstrate that after annealing at temperatures ranging from 700 °C to 1000 °C, 2D-diamond embedded within the graphene sheets emerges, and as the annealing temperature increases, the size of the 2D-diamond increases from approximately 15 nm to around 30 nm. When the annealing temperature reaches 1100 °C, no diamonds are found within the samples accompanied by larger Ta-containing compounds observed, confirming that monodisperse Ta atoms play a key role in graphene phase transition into 2D-diamond. This result provides a new approach for the synthesis of 2D-diamond in graphene at ambient pressure.

2. Materials and methods

A single batch of 0.5 g of multilayer graphene powder was placed into a mold with a diameter of 10 mm, and then compressed to form a pellet, as shown in Fig. 1(a). The upper limit of pressing force was set at 17.5 tons, while the lower limit was set at 7.5 tons, with a dwell time of 30 s. The mold was subjected to a pressure of 2226 MPa. The schematic diagram of the experimental process for depositing dispersed Ta atoms onto graphene sheets is shown in Fig. 1(b). The prepared graphene sheets were placed into the HFCVD reaction chamber, where the hydrogen gas flow rate was maintained at 200 sccm, the deposition pressure at 3.0 kPa, and the deposition power at 400 W for a duration of 15 min. Ta atoms were deposited onto the surface of the multilayer graphene substrate using a dual-spiral tantalum wire as the heating element. Upon completion of the deposition, the heating wire voltage was gradually reduced to 0 V at a rate of 2 V/min, finalizing the sample preparation. The prepared Ta-loaded graphene samples were annealed at 700 °C–1100 °C for 30 min using muffle furnace, as shown in Fig. 1(c).

The surface morphology was characterized by scanning electron microscope (SEM, HITACHI, Japan). The phase composition of the samples was characterized using a micro-confocal laser Raman spectrometer (with an excitation wavelength of 532 nm, model Renishaw inVia Reflex) from Renishaw. The microstructure, diffraction pattern, and EDS analysis of the samples were characterized by transmission electron microscope (TEM, Thermo Fisher Scientific, USA). The bonding state of the samples was analyzed with x-ray photoelectron spectroscopy (XPS, Kratos, Japan).

3. Results and discussion

As illustrated in Figs. 1(d)–1(i), field emission scanning electron microscopy (FESEM) was employed to characterize the morphologies of untreated graphene sheets and samples annealed at various temperatures. Figure 1(d) exhibits the morphology of an untreated graphene sheet sample, which displays a complete distribution of thin sheets stacked under pressure, with sheet sizes ranging from 0.5 μm to 3 μm. Figure 1(e) displays a sample annealed at 700 °C in a vacuum-sealed tube, where cracks begin to emerge on the surface of the graphene sheets, accompanied by localized delamination, although the layered structure remains largely unchanged. This indicates that annealing at lower temperatures has minimal impact on the structure of the graphene sheets. Figure 1(f) presents a sample annealed at 800 °C for 30 min, where the grooves on the surface of the graphene sheet layers become more pronounced, and the stacked structure of the graphene sheets becomes distorted and less well-defined. Figure 1(g) depicts a sample annealed at 900 °C for 30 min, where it is noteworthy that crystalline agglomerations start to appear on the surface of the graphene sheet layers, and the cracks deepen to the point of disconnection from each other. Figures 1(h) and 1(i) show samples annealed at 1000 °C and 1100 °C for 30 min, respectively. The images reveal that as the annealing temperature increases, the crack gaps on the surface of the graphene sheets widen, and the crystalline agglomerations thicken. These results suggest that as the annealing temperature gradually rises, the surface graphene sheet layers gradually fragment, and granular crystals precipitate out after annealing above 900 °C.

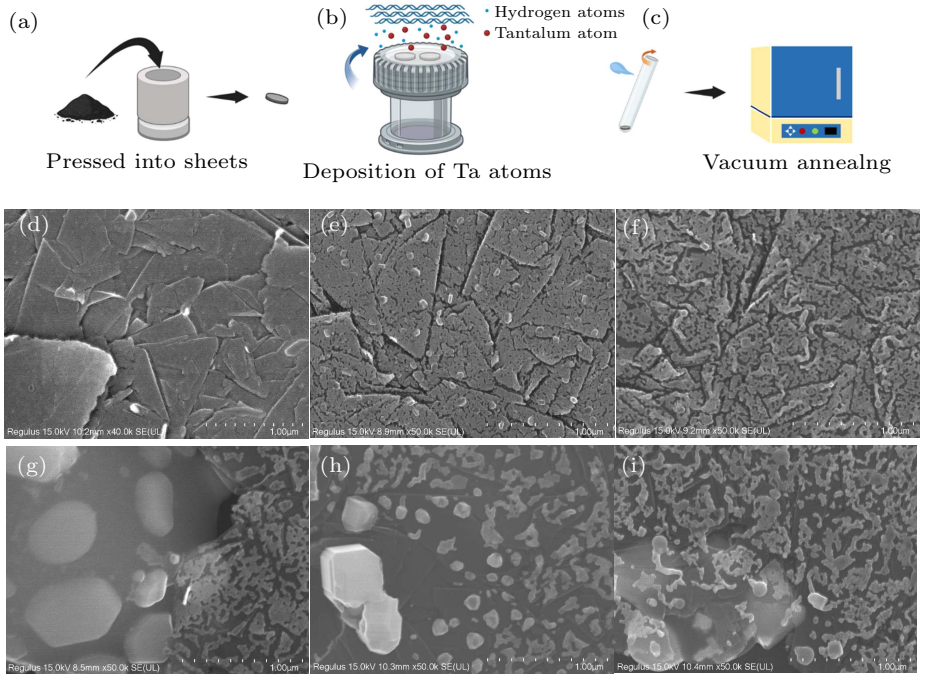


Fig. 1. Schematic diagrams of (a) graphene compression, (b) deposition of dispersed Ta atoms onto graphene sheets, and (c) vacuum annealing. Surface morphology of the samples (d) before vacuum sealed tube annealing, and annealed at (e) 700 °C, (f) 800 °C, (g) 900 °C, (h) 1000 °C, and (i) 1100 °C.

To investigate the changes in phase composition on the surface of multilayer graphene sheets after annealing at different temperatures, Raman spectroscopy was performed on this series of samples under excitation with light at a wavelength of 532 nm. Figure 2(a) shows the Raman spectra of the samples annealed at various temperatures. Four characteristic peaks were detected in all samples at 1350 cm^{-1}, 1580 cm^{-1}, 1620 cm^{-1}, and 2690 cm^{-1}. The peak at 1350 cm^{-1} corresponds to the D peak, associated with defects in the graphitic plane, while the peak at 1580 cm^{-1} is the G peak, related to sp^2 bonded carbon. The peak at 1620 cm^{-1} represents the D′ peak, indicative of edge defects in the vertically oriented graphene layers. The peak at 2690 cm^{-1} is the 2D peak, corresponding to the overtone of the D peak and indicative of single or few-layer graphene phonons. The Raman spectra of this group of samples exhibit typical characteristics of graphene, with no Raman signal detected at 1332 cm^{-1} that would indicate the presence of diamond.

Further analysis of the Raman spectra was conducted by comparing the intensity ratios of the fitted peaks. Figures 2(b) and 2(c) present the fitting results of the Raman spectra for the samples. The ratio of I_D/I_G was used to assess the variation in defects within the samples, while $FWHM_{2D}$, $FWHM_G$, and I_{2D}/I_G indicate changes in the number of graphene layers. The trend observed in the fitted data presented in Fig. 2(b) reveals that when Ta atoms are deposited onto the precursor multi-

layer graphene sheets using a CVD system, the I_D/I_G ratio increases, indicating that the deposition of Ta atoms introduces additional defects in the graphene, compromising the integrity of the graphene layers. After annealing at 700 °C, there is a decrease in the I_D/I_G ratio, suggesting that the defects of the graphene were partially repaired. Following annealing treatment at 800 °C, the I_D/I_G ratio decreased significantly, indicating further repair of the defects in the graphene and suggesting a change in the graphene structure, which may result in an increase in the ratio of sp^3 to sp^2 carbon content in the samples. When the annealing temperature is increased to 900 °C, the I_D/I_G ratio exhibits a slight increase compared to that at 800 °C. As the temperature further increased, the I_D/I_G ratio rose slightly, indicating that excessively high temperatures led to an increase in defects in the graphene.

It is also observed that after deposition Ta on graphene, the $FWHM_G$ undergoes a significant reduction, which is attributed to an increase in the degree of graphitization subsequent to Ta deposition. Following annealing, the $FWHM_G$ exhibits an initial increase followed by a decrease. At an annealing temperature of 700 °C, the precipitation of Ta between graphene layers introduces lattice distortion in the graphite, leading to an increase in $FWHM_G$. As the annealing temperature rises further, the $FWHM_G$ gradually decreases, suggesting a reduction in phonon scattering and an improvement in crystallinity within the graphene samples. This may be due to the gradual precipitation of the deposited Ta atoms as the annealing temperature increases. The trends in $FWHM_{2D}$ and I_{2D}/I_G shown in Fig. 2(c) indicate that after depositing Ta onto the multilayer graphene sheets via hot-wire CVD and subsequent annealing at temperatures below 1000 °C, the number of graphene layers increased. However, when the annealing temperature exceeded 1000 °C, the number of layers decreased.

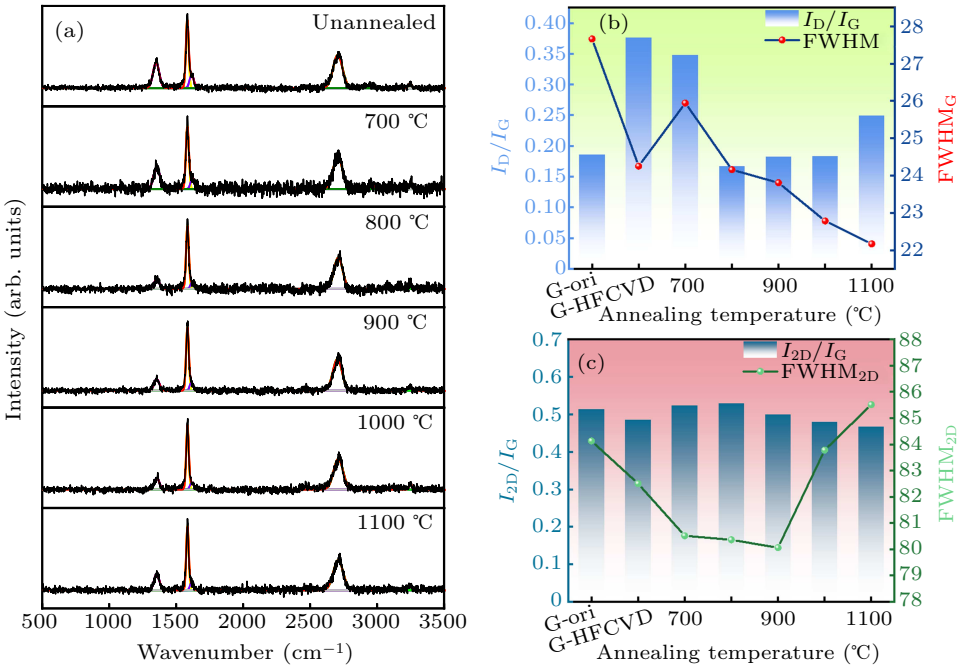


Fig. 2. (a) Raman spectra of untreated samples and annealed samples at different temperatures, variation of (b) I_D/I_G ratio and $FWHM_G$ and (c) I_{2D}/I_G ratio and $FWHM_{2D}$ with annealing temperature for the samples.

The phase structure of the samples was further characterized using high-resolution transmission electron microscopy (HRTEM). Figures 3(a) and 3(c) present the low-magnification transmission electron microscope (TEM) images of the samples after annealing under vacuum in sealed tubes at 700 °C for 30 min. Figure 3(a) reveals a high-contrast "arrowhead-shaped" region in the graphene sheet, accompanied by an agglomerated particle region. The selected area electron diffraction (SAED) pattern (SAED-a) of this region in Fig. 3(a) indicates the presence of (110) and (101) planes of graphite; these planes correspond to weaker stripes with smaller interplanar spacings, distributed across a large contiguous area. Through energy dispersive spectroscopy-mapping (EDS-Mapping) analysis of the distribution of C, O, and Ta elements in a partial area of Fig. 3(a), and comparison with the high-brightness small particles in high-angle annular dark field (HAADF) imaging and the distribution maps of C, O, and Ta elements, it is found that the sample surface is primarily enriched with C elements, i.e., the graphene substrate. The "arrowhead-shaped" region corresponds to the overlapping area of Ta and O elements, suggesting a high concentration of both Ta and O elements in this region. In the vicinity of the "arrow-shaped" region, there also exist a large number of dispersed Ta atoms. Figure 3(b) shows the high-magnification analysis near the "arrowhead-shaped" region. The fast Fourier transform (FFT) pattern (FFT-b) of this region displays two

pairs of diffraction spots with interplanar spacings of 0.206 nm and 0.251 nm, corresponding to the yellow particulate regions in Fig. 3(b). Due to their limited shape and lower contrast compared to the large-area sheet-like graphene substrate, combined with fourier transform (FT) analysis of the magnified yellow regions, it is determined that these two areas correspond to the (111) plane of particulate diamond with an interplanar spacing of 0.206 nm and a size range of 8 nm–12 nm, and the (110) plane of particulate diamond with an interplanar spacing of 0.251 nm and a size range of 10 nm–12 nm, respectively. Based on the observation from figure HAADF-I, it is noted that diamonds emerge in the regions where tantalum elements are relatively concentrated on the graphene layers.

Figure 3(c) exhibits a minor stacking phenomenon occurring in the graphene sheet. The SAED-c of this region reveals the presence of the (002), (101), and (110) planes of graphite, with the (002) plane corresponding to the larger curved lattice stripes observed in the sample. Figure 3(d) presents a high-magnification image of the d region in Fig. 3(c). The FFT-d of this area displays distinct graphite (002) and (100) planes, corresponding to the green region, along with a pair of diffraction spots with an interplanar spacing of 0.206 nm, corresponding to the yellow region. The yellow region appears as flakes embedded within the graphene layers, exhibiting localized presence rather than the extensive coverage of the graphene substrate. Upon magnifying the area labeled as 3, it is confirmed that the interplanar spacing of 0.206 nm matches the diffraction information of the (111) plane of diamond, suggesting a 2D-diamond thin layer with a size of approximately 10 nm–15 nm. Figure 3(e) displays a high-magnification image of the e region in Fig. 3(c). The FFT pattern (FFT-e) of this area shows clear graphite (002) and (100) planes, corresponding to the green region, and a pair of diffraction spots with an interplanar spacing of 0.126 nm, corresponding to the yellow region. Upon magnifying the yellow area labeled as 4, it is found that the interplanar spacing of 0.126 nm aligns with the diffraction information of the diamond (220) plane. This region, unlike the extensive graphene layers, exhibits localized presence and is identified as a 2D layered structure of diamond with a size of 10 nm–20 nm, embedded within the graphene layers. These 2D-diamonds observed via TEM are located in the regions of the graphene sheets where monodispersed Ta atoms are abundant, suggesting that Ta atoms facilitate the phase transformation of graphene into 2D-diamond after 700-°C annealing.

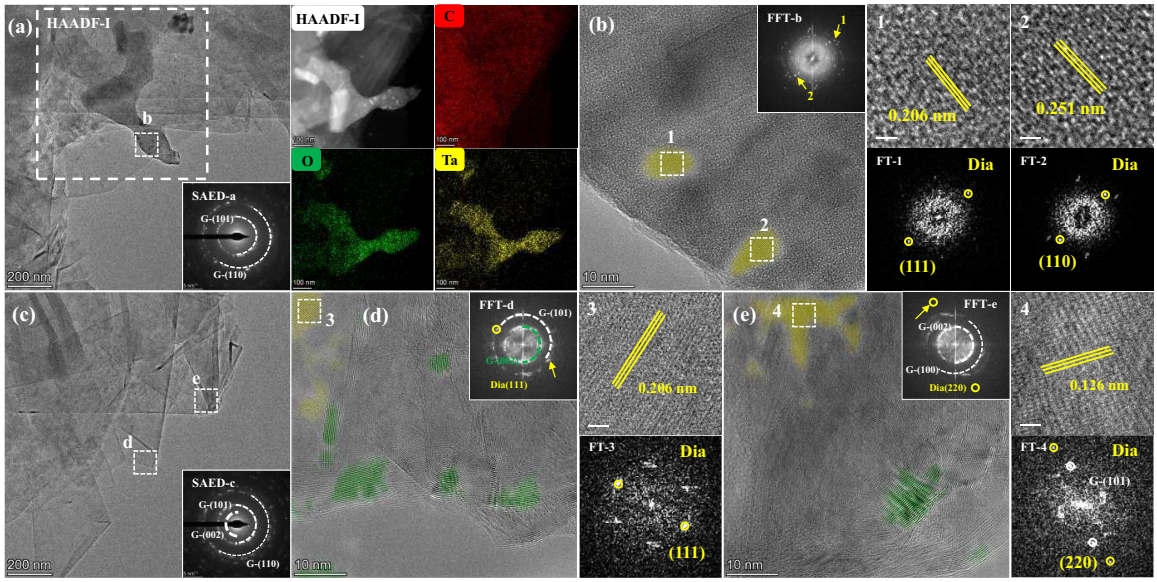


Fig. 3. (a) and (c) The low-magnification HRTEM images with inset SAED images of sample annealed at 700 °C for 30 min; HAADF-I is the HAADF image with EDS spectra of C, O, and Ta for the area indicated by the dashed box in panel (a). (b) high-magnification image of the area within the dashed box b in panel (a) with an inset FFT image; 1–2 magnified views of the boxed areas 1–2 in panel (b) along with their corresponding FT images; (d) and (e) high-magnification images of the dashed boxes d and e in panel (c) with their inset FFT images; 3 magnified view of the boxed area 3 in panel (d) along with its corresponding FT image, and 4 magnified view of the boxed area 4 in panel (e) along with its corresponding FT image.

Figures 4(a) and 4(c) present low-magnification TEM images of the sample after annealing at 800 °C for 30 min in a vacuum-sealed tube. In Fig. 4(a), the graphene sheets exhibit a reticulated morphology, accompanied by aggregated particles with darker contrast. The SAED pattern (SAED-a) of this region shows diffraction information predominantly from the (002) and (100) planes of graphite, as well as a plane with an interplanar spacing of 0.206 nm. Further analysis of the distribution of C, O, and Ta elements in this region is conducted using EDS-Mapping. By comparing the bright small particles in the HAADF image with the distribution maps of C, O, and Ta elements, it is found that the reticulated area is primarily composed of graphene, with O and Ta elements relatively dispersed within it. The darker contrast particle areas corre-

spond to aggregates of Ta–O. This indicates that the Ta atoms deposited on the graphene sheets are partially oxidized. Figure 4(b) shows a high-magnification analysis of the reticulated area b. The FFT-b in Fig. 4(b) displays diffraction information from the (002) plane of graphite, corresponding to the green region in Fig. 4(b), and a plane with an interplanar spacing of 0.206 nm, corresponding to the yellow region in Fig. 4(b). Upon magnifying region 1 in Fig. 4(b), it is found that these two pairs of interplanar spacings are 0.206 nm and 0.207 nm, respectively, with an angle between the planes of 70.2°, which matches the diffraction information of the (111) plane of diamond. The yellow lattice area appears as a 2D lamellar structure embedded within the interstitial spaces of the reticulated graphene area, with a size range of 15 nm–20 nm. It is observed that in Fig. 4(b), the 2D-diamond is found in the regions with Ta atoms, suggesting that Ta atoms facilitate the phase transformation of graphene into diamond, forming 2D-diamond. Also, in this region, there are O atoms observed, which prefered to improve the pahse transition according to our theoretical results.[22,24]

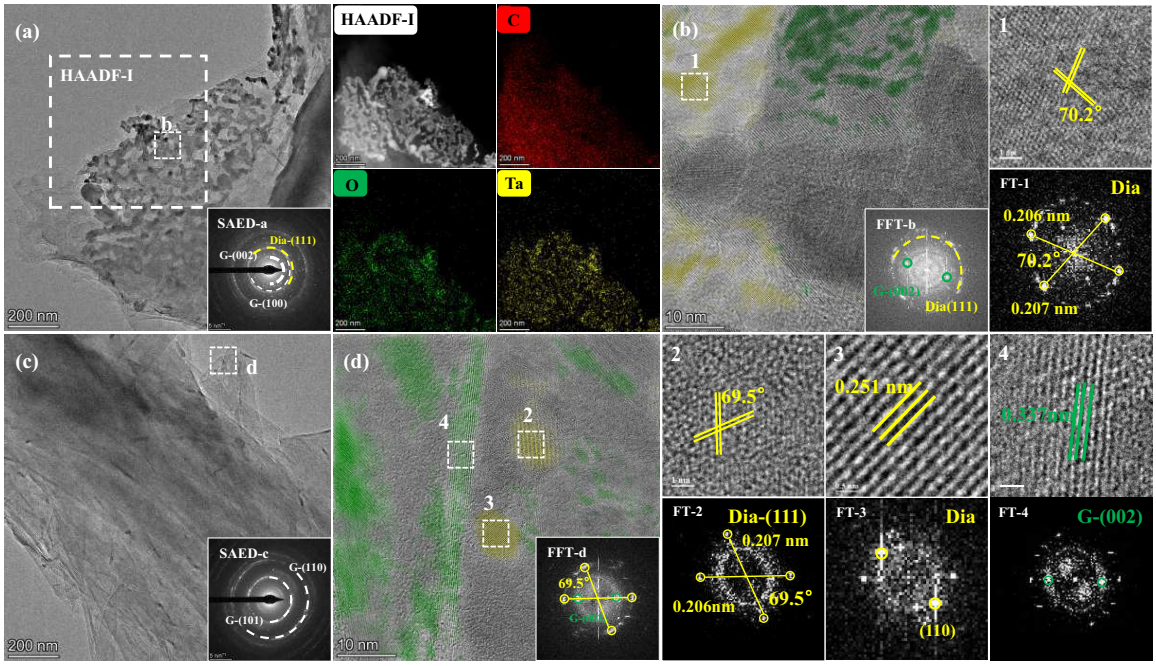


Fig. 4. (a) and (c) The low-magnification HRTEM images of the sample annealed at 800 °C for 30 min with inset SAED images. HAADF-I is the HAADF image of the area marked by the dashed box in panel (a), accompanied by the EDS spectra of C, O, and Ta elements for that area; (b) high-magnification image of the dashed box b in panel (a) with an inset FFT image; 1 magnified view of the area marked by the dashed box 1 in panel (b) along with its corresponding FT image; (d) high-magnification image of the dashed box d in panel (c) with an inset FFT image; 2–4 magnified views of the boxed areas 2, 3, and 4 in panel (d) along with their corresponding FT images.

Figure 4(c) displays the stacked ribbon structure of graphene. The SAED-c indicates the presence of diffraction information from the (110) and (101) planes of graphite in the region shown in Fig. 4(c). Figure 4(d) presents the high-magnification analysis result of the region d of the graphene sheet. The FFT-d in Fig. 4(d) shows diffraction information predominantly from the (002) plane of graphite, indicated by the green region, and lattice spacings of 0.206 nm and 0.207 nm corresponding to the diffraction from the (111) plane of diamond, indicated by the yellow region. Upon magnifying regions 2, 3, and 4 in Fig. 4(d), two particulate regions distinct from the graphite stripes are observed, namely, regions 2 and 3. Further magnifying these particulate regions, figure FT-2 reveals the existence of two pairs of interplanar spacings, 0.206 nm and 0.207 nm, respectively. The angle between these two pairs of crystal planes is 69.5°, leading to the conclusion that they represent the (111) plane of diamond, with a size range of 8 nm–12 nm and embedded in a particulate form within the graphene sheet layers. For the particulate in Fig. 4-3 that is enlarged and measured, its interplanar spacing is 0.251 nm. Since graphite is distributed in ribbon or platelet forms, it is postulated to be the (111) plane of diamond, with a size of 10 nm–12 nm, embedded between the graphene sheet layers surrounding the graphite ribbons. When the ribbon region in Fig. 4-4 is magnified, the measured interplanar spacing is 0.337 nm, corresponding to the (002) plane of graphite. These results indicate that when the annealing temperature reaches 800 °C, a layer of 2D-diamond with a size range of 15 nm–20 nm emerges within the graphene sheets.

Figures 5(a) and 5(c) present low-magnification TEM images of samples after annealing at 900 °C for 30 min in a vacuum-sealed tube. The SAED-a pattern indicates the presence of diffraction information from the (100) plane of graphite in this region, as well as diffraction information with interplanar spacings of 0.206 nm and 0.105 nm, which correspond to the (111) plane and the higher-order (222) plane

of diamond, respectively. Therefore, it is judged that this is the diffraction information of the (111) and (222) planes of diamond. Further analysis was conducted by magnifying the particle area in Fig. 5(a), as shown in Fig. 5(b). The FFT-b pattern reveals two pairs of diffraction spots with an interplanar spacing of 0.206 nm and an angle of 70.5° between them, corresponding to the yellow region in the Fig. 5(b), which is identified as diffraction information from the (111) plane of diamond. Simultaneously, diffraction fringes with an interplanar spacing of 0.258 nm are found in the darker-contrast particle, corresponding to the red region in Fig. 5(b), which matches the diffraction information of the (111) plane of TaC, leading us to conclude that this is the diffraction information of the (111) plane of TaC. After magnifying the selected areas of 1, 2, 3, 4 in Fig. 5(b), figure 5(b)-1 displays two pairs of diffraction spots with spacings of 0.206 nm and an angle of 70.5° between them, consistent with the diffraction information of the (111) plane of diamond. These spots manifest as 2D flakes embedded within the graphene thin layers, with a size range of 20 nm–30 nm. Figure 5(b)-2 also shows two pairs of diffraction spots with the same spacings and angle, corresponding to the (111) plane of diamond, with a similar size range. Figure 5(b)-3 displays two pairs of planes with a spacing of 0.206 nm and an angle of 70.5°, matching the diffraction information of the (111) plane of diamond, and a size range of 10 nm–15 nm. Figure 5(b)-4 shows a pair of planes with a spacing of 0.258 nm and a darker contrast, which we identify as the (111) plane of TaC, with a particle size of 10 nm–12 nm. As shown in Figs. 5-1, 5-2, and 5-3, the diamonds discovered are predominantly concentrated around tantalum-containing particles located at the graphene thin layer interfaces. This phenomenon further validates that within the graphene, after some Ta atoms undergo bonding and agglomeration, the residual small amount of Ta enhances its monodispersion, thereby facilitating the phase transformation of graphene into diamond.

Figure 5(c) displays a significant number of small particles observed on the graphene sheets, with diameters ranging from 15 nm to 40 nm. The SAED-c pattern indicates the presence of diffraction information from the (002) and (112) planes of graphite, as well as a pair of planes with an interplanar spacing of 0.207 nm and an angle of 71° between them, which corresponds to the diffraction information of the (111) plane of diamond in this region. HAADF-I with EDS spectra of C, O, and Ta for the area indicated by the dashed box in Fig. 5(c) suggests that tantalum and oxygen atoms are distributed on the sample surface, playing a crucial role in the phase transition.

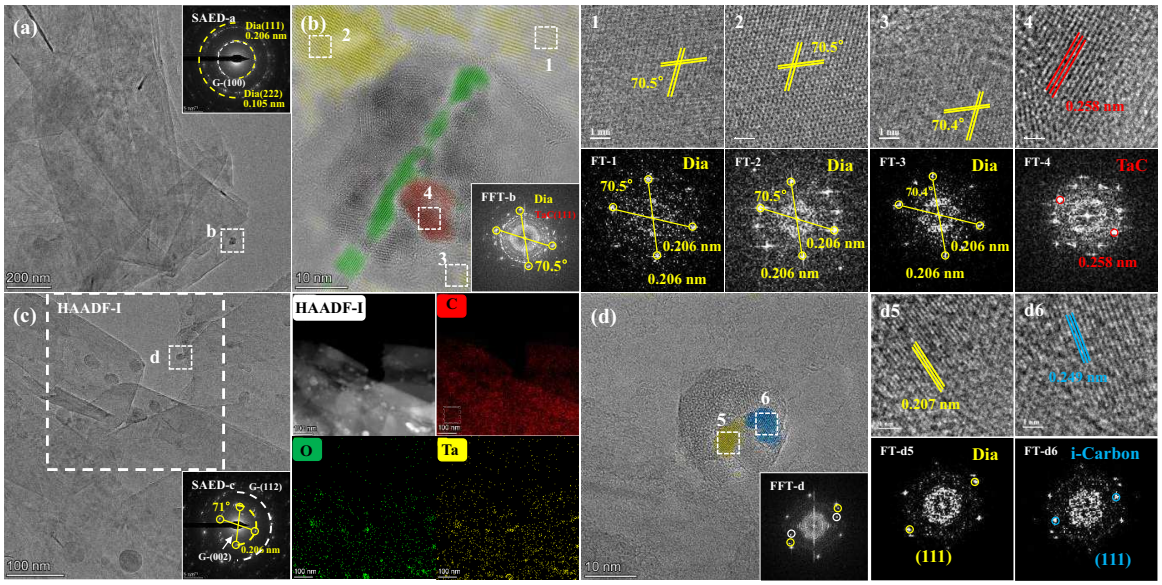


Fig. 5. (a) and (c) The low-magnification HRTEM images with their inset SAED images of the sample annealed at 900 °C for 30 min. (b) The high-magnification image of panel (a) with the inset of FFT image, and 1–4 the zoomed-in view of the boxed areas 1–4 in panel (b) with their corresponding FT images; HAADF-I is the HAADF image with EDS spectra of C, O, and Ta for the area indicated by the dashed box in panel (c); (d) the high-magnification image of dashed box d in panel (c) with the inset of FFT image; 5(d)-5–5(d)-6 enlarged view for the boxed areas 5 and 6 in panel (d) with their corresponding FT images.

Further analysis is conducted by magnifying particle d in Fig. 5(c). The FFT-d pattern reveals standard diffraction spots of the hexagonal rings of graphite, along with two pairs of diffraction spots that differ from those of graphite. Figures 5(d)-5 and 5(d)-6 exhibit magnified views of the interior of the amorphous particles. Figure 5(d)-5 displays diffraction information from the (111) plane of diamond, with an interplanar spacing of 0.207 nm, corresponding to the yellow region in the Fig. 5(d). These diffraction spots are present as 8–10 nm particles within the amorphous carbon spheres, leading us to conclude that they represent the (111) plane of diamond. Figure 5(d)-6 shows diffraction spots with an interplanar spacing

of 0.249 nm, corresponding to the blue region in Fig. 5(d). The blue striped area, with a particle size range of 10 nm–13 nm and low contrast, matches the diffraction information of the (111) plane of i-carbon.[29] These results indicate that after annealing at 900 °C, 2D-diamond with a size range of 10 nm–30 nm and some i-carbon is observed to be embedded within the layers of the graphene sheets, surrounding Ta-containing particles.

Figures 6(a) and 6(d) present the low-magnification TEM images of samples after annealing at 1000 °C for 30 min. The SAED-a pattern in Fig. 6(a) indicates the presence of diffraction information originating predominantly from the graphite (101) plane, along with interplanar spacings of 0.145 nm and 0.072 nm, which we interpret as diffraction from the diamond (112) plane and its higher-order diffraction plane (224), respectively. Further analysis was conducted by magnifying regions b and c in Fig. 6(a). FFT-b reveals a pair of distinct diffraction spots corresponding to the graphite (002) plane, indicated by the green area in Fig. 6(b), arranged in a common stripe-like pattern, along with a pair of diffraction spots with an interplanar spacing of 0.206 nm, corresponding to the yellow-colored sections. Upon magnifying region 1 in Fig. 6(b), the measured interplanar spacing of 0.206 nm corresponds to the diffraction information of the diamond (111) plane. These diamond structures, ranging in size from 20 nm–25 nm, exhibit a 2D platelet-like morphology adjacent to the graphite (002) stripes and embedded between the graphene sheets. In contrast, figure 6(c) displays amorphous carbon spheres with a size range of 50 nm–60 nm. This is attributed to the diffusion of tantalum atoms at high temperatures, which facilitated the conversion of graphene into amorphous carbon.[26]

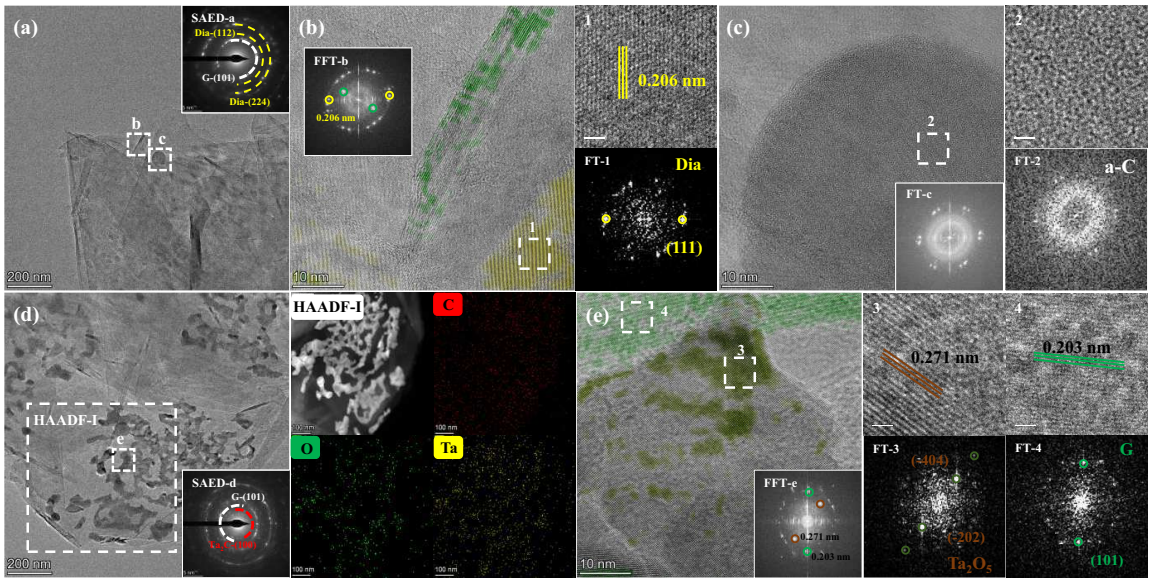


Fig. 6. (a) and (d) Low-magnification HRTEM images of sample annealed at 1000 °C for 30 min with inset SAED images; (b) high-magnification image of the dashed box b in panel (a) with an inset FFT image; 1 magnified view of the area marked by the dashed box 1 in panel (b) along with its corresponding FT image; (c) high-magnification image of the dashed box c in panel (a) with an inset FFT image; 2 magnified view of the area marked by the dashed box 2 in panel (c) along with its corresponding FT image. HAADF-I is the HAADF image of the area marked by the dashed box in panel (d) accompanied by the EDS spectra of C, O, and Ta elements for that area; (e) high-magnification image of the dashed box e in panel (d) with an inset FFT image; 3–4 magnified views of the boxed areas 3 and 4 in panel (e) along with their corresponding FT images.

Figure 6(d) exhibits a significant amount of network-like agglomeration morphologies observed on the graphene sheets. The SAED-d pattern indicates the presence of diffraction information originating from both the graphite (101) plane and the Ta_2C (100) plane within this region. By analyzing the EDS-mapping images of this area and further examining the distribution of C, O, and Ta elements, a comparison between the bright small particles in the HAADF image and the distribution maps of C, O, and Ta elements reveals overlapping distribution areas of Ta and O elements on the sample surface, with both elements being relatively dispersed. Further analysis is conducted by magnifying region e in Fig. 6(d). Upon magnifying regions 3 and 4 in Fig. 6(e), two sets of diffraction information are observed in Fig. FT-3. The measured interplanar spacings of these two sets of planes are 0.271 nm and 0.135 nm, respectively, and the angle between them is 0°, corresponding to the (–202) plane and the higher-order (–402) plane of Ta_2O_5, respectively. Therefore, we identify this as Ta_2O_5, indicating that an increase in annealing temperature promotes the oxidation of Ta. Additionally, there is a significant amount of diffraction originating from the graphite (101) plane, suggesting that Ta_2O_5 agglomerates are distributed on the surface of graphene sheets. The above results suggest that after annealing at 1000 °C, diamond platelets with sizes ranging from 20 nm–25 nm and amorphous carbon spheres with sizes ranging from 50 nm–60 nm emerge within the graphene sheet layers. Simultaneously, the elevated temperature exacerbates the oxidation of Ta between graphene layers.

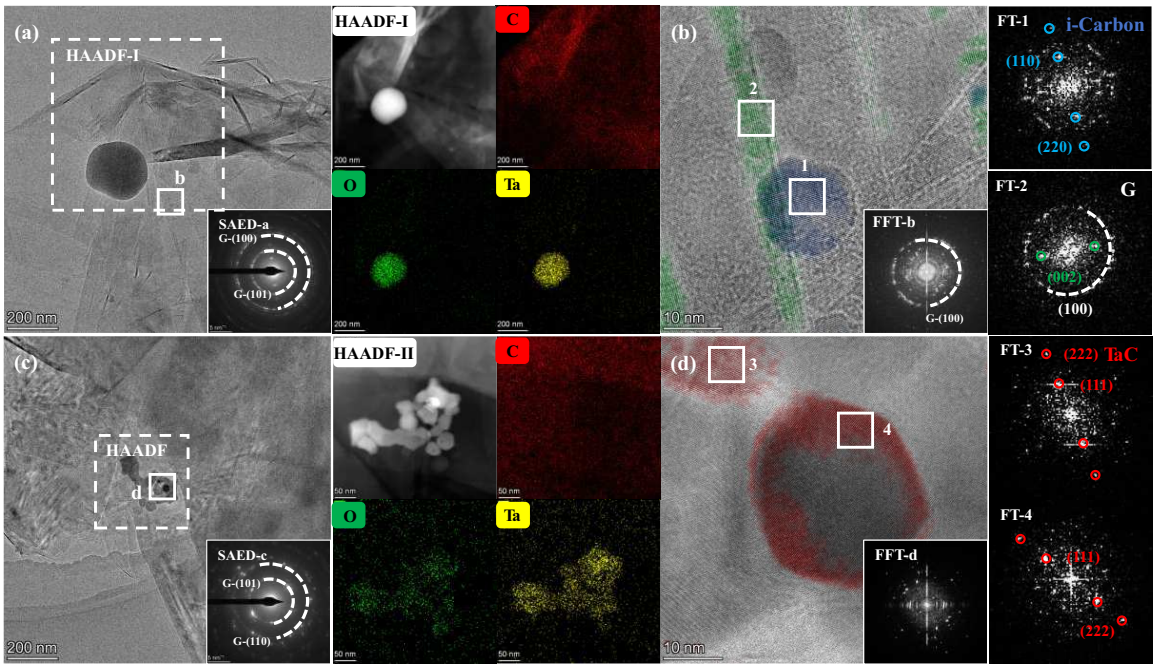


Fig. 7. (a) and (d) The low-magnification HRTEM images after vacuum sealing treatment at 1100 °C for 30 min, with inset SAED images; HAADF-I is the HAADF image of the area marked by the dashed box in panel (a) accompanied by the EDS spectra of C, O, and Ta elements for that area; (b) high-magnification image of panel (a) with an inset FFT image; FT-1 and FT-2 are the FT images of the boxed areas 1–2 in panel (b), respectively. HAADF-II is the HAADF image of the area marked by the dashed box in panel (c) accompanied by the EDS spectra of C, O, and Ta elements for that area. (d) High-magnification image of the boxed area d in panel (c) with an inset FFT image; FT-3 and FT4 are the FT images of the boxed areas 3 and 4 in panel (d), respectively.

Figures 7(a) and 7(c) present low-magnification TEM images of samples after annealing at 1100 °C for 30 min in a vacuum-sealed tube. In Fig. 7(a), particles with relatively dark contrast and sizes ranging from 150 nm–170 nm are observed on the graphene sheets. The SAED-a pattern indicates the presence of diffraction information originating from the graphite (101) and (110) planes in this region. By analyzing the EDS mapping images of this area and further examining the distribution of C, O, and Ta elements, a comparison between the bright small particles in the HAADF image and the distribution maps of C, O, and Ta elements reveals overlapping distribution areas of Ta and O elements on the sample surface. This suggests that Ta atoms deposited on the graphene sheets have been oxidized, forming TaO_x agglomerates with spherical sizes of approximately 200 nm. Further analysis is conducted by magnifying region b in Fig. 7(a). The FFT-b pattern displays diffraction information from the graphite (100) plane. Upon magnifying the particle region in Fig. 7(b), the diffraction information corresponds to the (110) and (220) planes of i-carbon, with particle sizes ranging from 25 nm–30 nm. This is due to the significant reduction in the number of monodisperse tantalum atoms deposited within the graphene layers during the high-temperature annealing process at 1100 °C. Consequently, the transformation of graphene into the diamond phase becomes difficult to achieve, resulting only in the formation of i-carbon. Additionally, as the annealing temperature increases, the diffusion capability of tantalum atoms enhances. These tantalum atoms diffuse into larger areas of graphene, thereby forming more and larger-sized i-carbon particles.

Figure 7(c) displays the presence of particulate agglomeration on graphene. The SAED-c pattern indicates the presence of diffraction information originating from the graphite (101) and (110) planes in this region. By analyzing the EDS mapping images of this area and further examining the distribution of C, O, and Ta elements, a comparison between the bright small particles in the HAADF image and the distribution maps of C, O, and Ta elements reveals overlapping distribution areas of Ta and O elements on the sample surface. This indicates an enrichment of Ta and O elements in this region. Further analysis was conducted by magnifying region d in Fig. 7(c). Two particulate regions distinct from the graphite stripes are observed in Fig. 7(d), labeled as regions 3 and 4, respectively. Upon magnifying these particulate regions, both Figs. 7(d)-3 and 7(d)-4 display the presence of two sets of TaC crystal planes, with particle sizes ranging from 30 nm–40 nm. Above results reveal that when the annealing temperature reaches 1100 °C, larger spherical i-carbon particles are formed. This indicates that significant chemical changes and interactions occur between Ta atoms and O within the graphene layers during the annealing process.

The x-ray photoelectron spectroscopy (XPS) tests were conducted on the samples, and the results were further analyzed in conjunction with TEM image analysis to investigate the relationship between the bonding changes and atomic content of oxygen (O) and tantalum (Ta) on the graphene surface and the formation of diamond. Figure 8(a) presents the fitted bonding spectrum of the C 1s peak for the samples, while fig-

ure 8(d) displays the trend in the proportion of sp^2 and sp^3 carbon bondings. The C 1s peaks of all samples can be fitted into four peaks located at 284 eV, 284.6 eV, 285.2 eV, 286.2 eV, and 287.3 eV, corresponding to sp^2 carbon, sp^3 carbon, C–O, C=O, and π–π^* bonds.[30–32] As illustrated in Figs. 8(a) and 8(d), as the annealing temperature increases from 700 °C to 900 °C, the sp^3 carbon content gradually increases, while the sp^2 carbon content remains relatively low. This trend is consistent with the TEM analysis results, which shows that the size of 2D diamonds increases from approximately 10 nm to 25 nm. However, when the annealing temperature rises to 1000 °C, XPS results indicate a decrease in sp^3 carbon content and a significant increase in sp^2 carbon content. Corresponding TEM results reveal a reduction in the size of 2D-diamond to approximately 20 nm, along with the observation of larger amorphous carbon spheres. As the annealing temperature further increases to 1100 °C, the sp^3 carbon content drops to its lowest level, while the sp^2 carbon content decreases slightly compared to that at 1000 °C. At this temperature, TEM results show the presence of i-carbon particles, but no diamond formation is observed.

Figure 8(b) presents the fitted bonding spectrum of the O 1s peak of the sample, while figure 8(e) reveals the trends in the proportions of lattice oxygen (O_a) and oxygen vacancies (O_v) with annealing temperature. When the annealing temperature exceeds 1000 °C, the O 1s peak shifts to a higher potential, indicating intensified internal oxidation of the sample. Combined with TEM results, it is observed that more TaO_x appears between graphene layers after annealing at temperatures above 1000 °C. During the annealing process from 700 °C to 900 °C, the O_a content gradually decreases, suggesting a partial reduction in the oxidation degree of Ta within the graphene layers. Simultaneously, the increase in O_v content implies the breaking of Ta–O bonds, particularly during annealing at 700 °C to 900 °C and 1100 °C. This promotes the enlargement of 2D diamond sizes. However, when the annealing temperature reaches 1000 °C, the O_a content rises again, indicating intensified oxidation. At an annealing temperature of 1100 °C, the O_a content decreases, as Ta combines with C between graphene layers to form TaC_x aggregations.

Figure 8(c) displays the fitted bonding spectrum of the Ta 4f peak, while figure 8(f) shows the trends in the atomic mass ratios of Ta 4f and O 1s with annealing temperature. When the annealing temperature exceeds 1000 °C, the Ta 4f peak shifts to a higher potential, indicating intensified oxidation of Ta on the graphene surface. As the annealing temperature increases, the surface concentrations of O and Ta gradually decrease, indicating an increase in the precipitation and agglomeration of Ta–O during the annealing process.

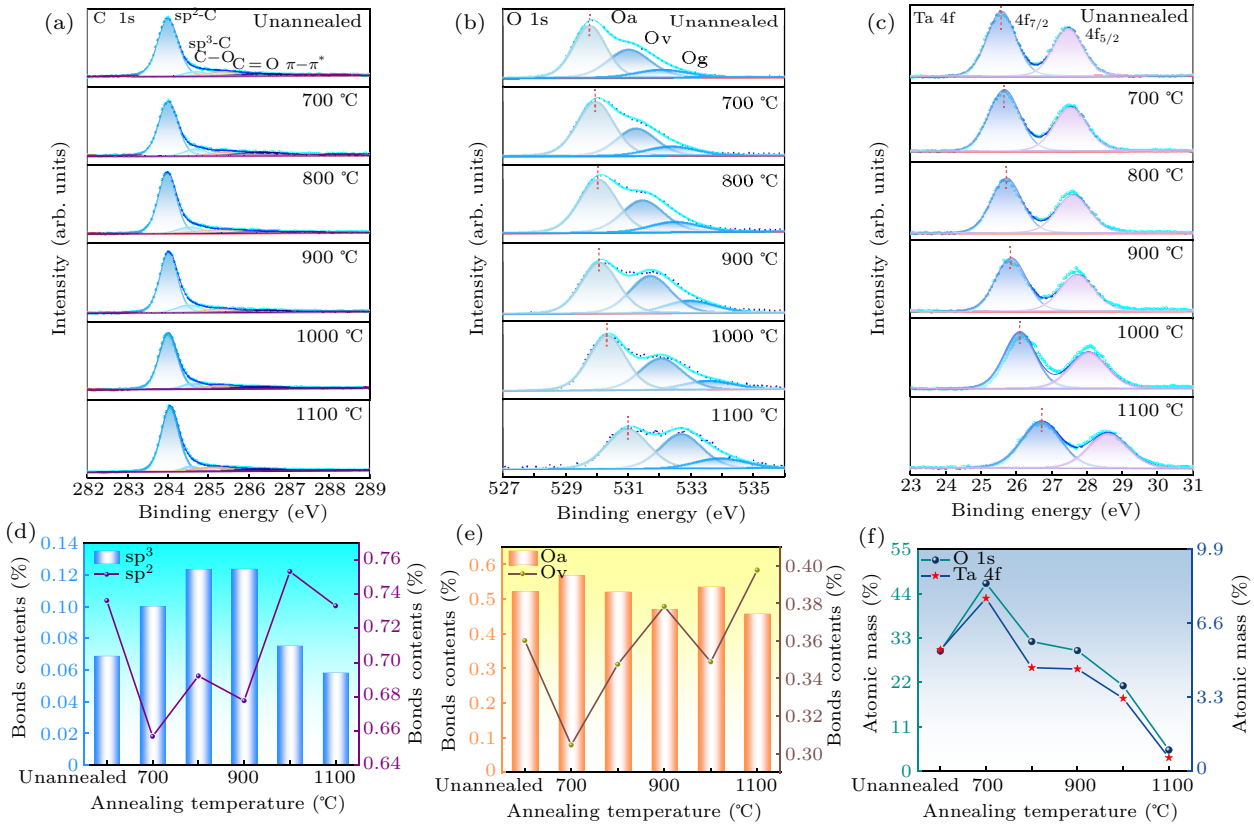


Fig. 8. (a) Core-level spectra of C 1s, (b) core-level spectra of O 1s, and (c) core-level spectra of Ta 4f for untreated samples and samples annealed at different temperatures, along with their fitting curve; Variation of (d) sp^2 and sp^3 carbon bond contents, (e) lattice oxygen (O_a) and oxygen vacancy (O_v) content, and (f) atomic mass of O 1s and Ta 4f on the sample surface with annealing temperatures.

The XPS analysis has unveiled the influence of annealing temperature variations on the chemical bonding and distribution state of Ta elements interlayers within graphene, which in turn significantly affects the phase transition process of graphene. Specifically, when the annealing temperature does not exceed 900 °C, the Ta–O content exhibits a decreasing trend as the temperature rises, accompanied by an increase in sp^3 carbon content. This indicates that Ta, when not bound to O, facilitates the transition of graphene towards the diamond phase. However, when the annealing temperature reaches 1100 °C, Ta binds with C and agglomerates, resulting in a decrease in the dispersion of Ta atoms and consequently hindering the progress of graphene's phase transition.

Combining TEM images and XPS data, we have observed that annealing temperature plays a crucial role in the phase transition of graphene. Under annealing conditions below 1000 °C, as the temperature increases, the sp^3 carbon content rises, and 2D-diamond thin regions emerge in the samples, with their sizes expanding as the annealing temperature further elevates. At this stage, Ta is not extensively bound to O and exists in a monomeric state with high dispersion, which favors the phase transition of graphene into 2D-diamond. However, when the annealing temperature rises further to 1000 °C and above, the contents of O_a and O_v exhibit trends of initial increase followed by decrease and initial decrease followed by increase, respectively, while the sp^3 carbon content decreases significantly. TEM images reveal that at 1000-°C annealing, large-sized TaO_x particles appear in the samples, accompanied by a reduction in diamond size. When the annealing temperature reaches 1100 °C, large-sized agglomerates of TaO_x and TaC_x are observed within the samples, with no diamond diffraction information detected. These observations indicate that the changes in Ta bonding and distribution state induced by annealing temperature are key factors influencing the catalytic transformation of graphene into the diamond phase.

4. Conclusion

In summary, graphene sheets decorated with monodisperse tantalum serve as phase transition precursors for the successful synthesis of 2D-diamond and through annealing treatments at various temperatures in a vacuum environment. Analysis using TEM and XPS reveals that monodisperse Ta atoms play a crucial role in facilitating the graphene phase transition during the annealing process. Our results indicate that the optimal annealing temperature is 900 °C, at which the size of the 2D-diamond increases to 20 nm–30 nm. However, when the annealing temperature is raised to 1100 °C, no diamond structure is observed in the samples, and significant agglomeration of tantalum compounds is found between the graphene layers. This suggests that excessively high annealing temperatures cause the monodisperse tantalum to precipitate out from the graphene sheets and combine with carbon and oxygen, thereby hindering the phase transition process. Our research findings provide conditions for the preparation of 2D-diamond from tantalum-loaded graphene under atmospheric pressure, which is of great significance for the development of using graphene as a precursor for the synthesis of 2D-diamond.

Acknowledgements

Project supported by the Key Project of the National Natural Science Foundation of China (Grant No. U1809210), the International Science Technology Cooperation Program of China (Grant No. 2014DFR51160), the One Belt and One Road International Cooperation Project from the Key Research and Development Program of Zhejiang Province, China (Grant No. 2018C04021), the National Natural Science Foundation of China (Grant Nos. 50972129, 50602039, and 52102052), the Fund from Institute of Wenzhou, Zhejiang University (Grant Nos. XMGL-CX-202305 and XMGL-KJZX-202307), and the Project from Tanghe Scientific & Technology Company (Grant No. KYY-HX-20230024).

References

[1] Achard J, Silva F, Issaoui R, Brinza O and Gicquel A 2011 *Diam. Relat. Mater.* **20** 145
[2] Friel I, Clewes S L, Dhillon H K, Perkins N and Scarsbrook G A 2009 *Diam. Relat. Mater.* **18** 808
[3] Betzel G T, Lansley S P, Mckay D and Meyer J 2012 *Med. Phys.* **691** 34
[4] Ryan M, Vijayan M, Flavia C, Settimio P and Arghya P 2016 *Front. Bioeng. Biotechnol.* **01** 585
[5] Hongdong L, Shaoheng C, Jia L and Jie S 2015 *J. Nanomater* **2015** 692562
[6] Sivek J, Leenaerts O, Partoens B and Peeters F M 2012 *J. Phys. Chem. C* **116** 19240
[7] Zhu L, Li W and Ding F 2019 *Nanoscale* **10** 4248
[8] Samarakoon D K and Wang X Q 2010 *Acs Nano* **4** 4126
[9] Sun Z, Zhang C, Qiu D, Gao N and Li H 2020 *Diam. Relat. Mater.* **101** 107641
[10] Cheng T, Liu Z and Liu Z 2020 *J. Mater. Chem. C* **39** 13819
[11] Gupta S, Yang J H and Yakobson B I 2019 *Nano Lett.* **19** 408
[12] Cai Z, Li B, Chen L, Wang Z, Fang S, Wang Y, Ma H and Jia X 2022 *Chin. Phys. B* **31** 108104
[13] Sofo J O, Chaudhari A S and Barber G D 2007 *Phys. Rev. B* **75** 153401
[14] Antipina L Y and Sorokin P B 2015 *J. Phys. Chem. C* **119** 2828
[15] Clark S M, Jeon K J, Chen J Y and Yoo C S 2013 *Solid State Commun.* **154** 15
[16] Grayfer E D, Makotchenko V G, Kibis L S, Boronin A I, Pazhetnov E M, Zaikovskii V I and Fedorov V E 2013 *Chem. Asian. J.* **8** 2015
[17] Jeon K J, Lee Z, Pollak E, Moreschini L, Bostwick A, Park C M, Mendelsberg R, Radmilovic V, Kostecki R, Richardson T J and Rotenberg E 2011 *Angew. Chem. Int. Ed.* **5** 1042
[18] Elias D C, Nair R R, Mohiuddin T M G, Morozov S V, Blake P, Halsall M P, Ferrari A C, Boukhvalov D W, Katsnelson M I, Geim A K and Novoselov K S 2009 *Science* **323** 610
[19] Diankov G, Neumann M and Goldhaber-Gordon D 2013 *Angew. Chem. Int. Ed.* **7** 1324
[20] Bakharev P V, Huang M, Saxena M, Lee S W and Ruoff R S 2020 *Nat. Nanotechnol.* **15** 59
[21] Chen C K, Fan D, Xu H, Jiang M Y, Li X, Lu S H, Ke C C and Hu X J 2022 *Carbon* **196** 466
[22] Jiang M Y, Chen C K, Wang P, Guo D F, Han S J, Li X, Lu S H and Hu X J 2022 *Proc. Natl. Acad. Sci. USA* **119** 2201451119
[23] Chen C K, Li Y, Guo D F, Ke C C, Fan D, Lu S H, Li X, Jiang M Y and Hu X J 2023 *ACS Appl. Mater. Interfaces* **15** 30684

[24] Lu S H, Zhang X T, Chen C K, Jiang M Y, Li X and Hu X J 2024 *J. Mater. Chem. A* **12** 27767
[25] Lu S H, Lei Y F, Zhu K and Hu X J 2025 *Carbon* **235** 120092
[26] Zhu Z G, Jiang C Q, Chen C K, Lu S H, Jiang M Y, Li X and Hu X J 2023 *Carbon* **211** 118098
[27] Zhu Z G, Chen C K, Lu S H, Li X and Hu X J 2025 *Adv. Sci.* **2025** 2411504
[28] Zhu Y H, Zhu Z G, Chen C K, Jiang M Y, Li X, Lu S H and Hu X J 2024 *Acta Phys. Sin.* **73** 028101 (in Chinese)
[29] Vora H and Moravec T J 1981 *J. Appl. Phys.* **52** 6151
[30] Yeo R J, Rismani E, Dwivedi N, Blackwood H, Tan H R, Zhang Z, Tripathy S and Bhatia C S 2014 *Diam. Relat. Mater.* **44** 100
[31] Dwivedi N, Yeo R J, Satyanarayana N, Kundu S, Tripathy S and Bhatia C S 2015 *Sci. Rep.* **5** 7772
[32] Rao X, Yang J, Chen Z, Yuan Y, Chen Q, Feng X, Qin L and Zhang Y 2020 *Bioact. Mater.* **5** 192